Generation of droplet arrays with rational number spacing patterns driven by a periodic energy landscape

Anatoly Rinberg, Georgios Katsikis, and Manu Prakash

Generation of droplet arrays with rational number spacing patterns driven by a periodic energy landscape

Anatoly Rinberg,[1] Georgios Katsikis,[2] and Manu Prakash[3]

[1] School of Engineering and Applied Sciences, Harvard University, Cambridge, Massachusetts 02138, USA
[2] Department of Mechanical Engineering, Stanford University, Stanford, California 94305, USA
[3] Department of Biongineering, Stanford University, Stanford, California 94305, USA
(Dated: August 23, 2017)

The generation of droplets at low Reynolds numbers is driven by non-linear dynamics that give rise to complex patterns concerning both the droplet-to-droplet spacing and the individual droplet sizes. Here we demonstrate an experimental system in which a time-varying energy landscape provides a periodic magnetic force that generates an array of droplets from an immiscible mixture of ferrofluid and silicone oil. The resulting droplet patterns are periodic, owing to the nature of the magnetic force, yet the droplet spacing and size can vary greatly by tuning a single bias pressure applied on the ferrofluid phase; for a given cycle period of the magnetic force, droplets can be generated either at integer multiples (1, 2, etc.), or at rational fractions (3/2, 5/3, 5/2, etc.) of this period with mono- or multidisperse droplet sizes. We develop a discrete-time dynamical systems model not only to reproduce the phenotypes of the observed patterns but also provide a framework for understanding systems driven by such periodic energy landscapes.

Discrete-time dynamical systems have been used to study physical phenomena such as population dynamics of predator-prey behavior [1, 2], spatial ecological patterns [3], control theory [4] and chaotic electronic circuits [5]. These systems often deal with recursive mathematical relations and use iterative maps to describe behaviors such as convergence to stable points, limit cycles and chaos [6–8].

In fluidic systems, droplet generation can be thought of as a discrete event, corresponding to the moment when a droplet breaks free from the bulk phase, making droplet generation well positioned to be studied as a discrete-time dynamical system. Indeed, droplet or bubble dynamics have been described using discrete-time approaches including not only the generation of droplets in dripping faucets [9] or bubbles in microchannels [10] but also the circulation of droplets in microfluidic networks [11, 12]. These descriptions are important given the significance of droplet generation either for technological purposes [13–16], or fundamental physical understanding. With regards to the latter, there is a conceptual connection between discrete-time dynamical systems and the study of droplet pattern generation, which relates the size of the droplets to their spacings, often revealing asymmetries even at low Reynolds numbers under laminar flow [17–19]. Such patterns further enable self-organization phenomena where generated droplets are driven into ordered structures [20, 21].

Unlike microchannel configurations for droplet generation [22] that induce shearing between the two phases through T-junctions [17, 18, 23] or flow focusing [24–26], where the timescales of droplet generation arise from balance between viscous and capillary forces, in this work, we report a novel microfluidic system with an intrinsic driving frequency determined by the time-varying magnetic energy landscape with a two-phase immiscible mixture of water-based ferrofluid (FF) and silicone oil. The magnetic energy landscape generates an oscillatory force that produces the droplet arrays whose patterns depend on the energy of breakup, the oscillation frequency and a bias flow-rate. The same concept of magnetic energy landscapes has previously been utilized to synchronously manipulate water-based FF droplets and, through droplet-to-droplet interactions, perform physical logic operations [27]. In this letter, we use this platform to demonstrate control over periodic droplet patterns, characterized by different droplet-to-droplet spacing and droplet sizes, and develop a discrete-time dynamical system model to explain the dynamics driving the formation of these patterns.

Experimental methods − We supply the FF through an inlet tubing (diameter $d_{tube} = 300 \ \mu m$) that is placed at a distance $d = 50 - 200 \ \mu m$ from a substrate covered with a $3 - 5 \ mm$ thick film of silicone oil (Fig. 1a, side view, and Section I in Appendix). The FF reservoir is held at a height h_{ff} from the substrate, that creates a differential pressure $\Delta P = \rho_{ff} \ g \ h_{ff}$, where $\rho_{ff} = 1.28 \ g/cm^3$ is the density of the FF and $g = 9.81 \ m/s^2$ is the acceleration of gravity. Due to this pressure, ΔP, there is flow of bulk FF with a rate Q.

The droplets are generated through the interaction of the bulk FF with soft-magnetic (permalloy) tracks (characteristic length $\sim 1 \ mm$) on the substrate via exposure to two magnetic fields. The first magnetic field, $\mid B_z \mid = 250 \ G$, is perpendicular to the substrate, has a fixed magnitude and polarizes the bulk FF in a uniform manner. The second magnetic field, $\mid B_{xy} \mid = 40 \ G$, is in the plane of the substrate, is rotating with a radial frequency ω and polarizes the tracks. As a result, these magnetic fields create a dynamic, spatiotemporal magnetic energy landscape, where the FF will be driven towards the minimization of its potential energy. To accomplish this, the lower end of the bulk is subject to a magnetic force $\overrightarrow{F}_{mag}$ that extracts sub-millimeter diameter droplets (Fig. 1a, side view). For this study, we
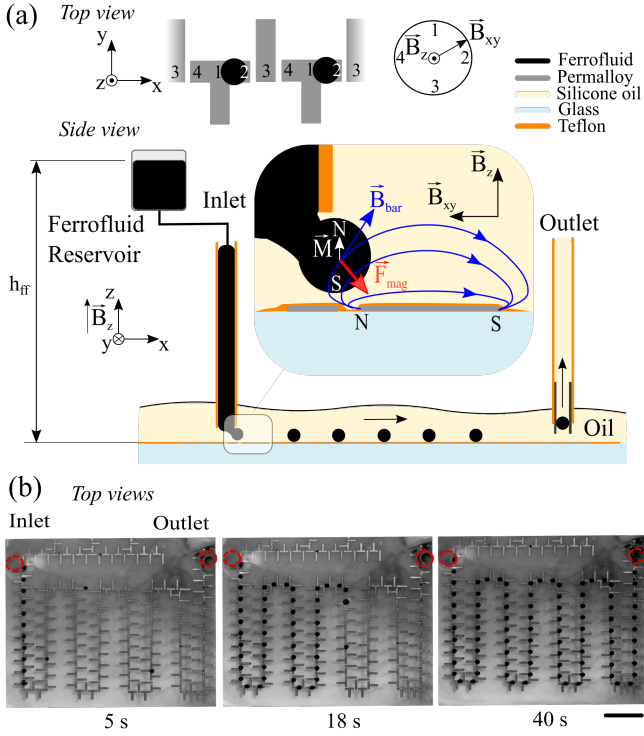
FIG. 1: (a) Schematic of the droplet generator. *Top view*: Periodic tracks of 'T' and 'I' permalloy bars (gray) with FF droplets (black) propagating under magnetic fields, $\vec{B}_z$, $\vec{B}_{xy}$. The numbers "1-4" on the bars correspond to the locations that the droplets occupy as $\vec{B}_{xy}$ obtains the angular orientations "1-4" [27]. *Side view*: Droplet array generated from reservoir with height, h_{ff}, via a magnetic force $\vec{F}_{mag}$ (red) from the coupling of the droplet magnetization $\vec{M}$ (white) with the magnetic field of the bar $\vec{B}_{bar}$ (blue). The letters 'N' and 'S' denote polarizations. (b) Top-view sequential snapshots of generated droplets propagating on winding tracks of 'T' and 'I' bars. Red dashed circles indicate the inlet and outlet. $B_z = 250 \ G$, $B_{xy} = 40 \ G$ at frequency $f = 2 \ Hz$. Scale bar 5 mm.

restrict ourselves to tracks that have shapes of 'T' and 'I' bars that ensure that they can be polarized effectively by the $\vec{B}_{xy}$ and suffice not only to generate droplets but also to propagate them along the tracks (Fig. 1a, top view). For a fixed position of the inlet tube, we show both droplet generation and propagation along the tracks of the substrate (Fig. 1b, top view, and Video 1 in Supplemental Material [28]). To avoid overcrowding the substrate with droplets, we use outlet lines connected to a negative pressure line that remove the droplets from the substrate (Fig. 1a, and Section I in Appendix).

Experimental observations − For given magnetic fields and fixed positions of the inlet and outlet tubes, we apply pressures in the range $\Delta P = 0.5 - 8 \ kPa$. We observe that the system is in a constant flow and pressure regime (Section I in Appendix) and generates droplet arrays converging to a steady-state pattern within 2-3 cy-
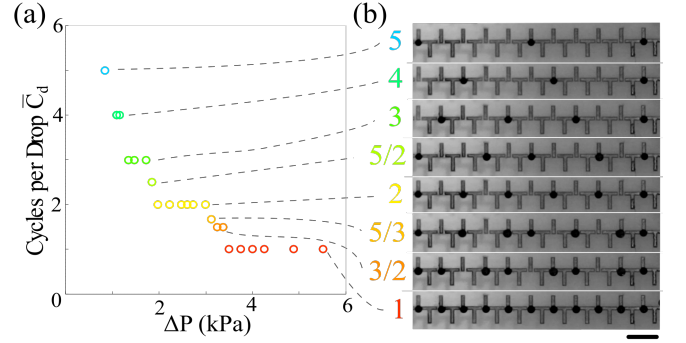

FIG. 2: (a) Plot of $\bar{C}_d$, the average number of cycles of $\vec{B}_{xy}$ needed to generate a droplet, versus the hydrostatic pressure ΔP. (b) Snapshots from the experiments of (a) with droplet-to-droplet spacings corresponding to different $\bar{C}_d$ values. $B_z = 250 \ G$, $B_{xy} = 40 \ G$, $f = 2 \ Hz$. Scale bar 2 mm.

cles of $\vec{B}_{xy}$. After converging to a steady-state pattern, we define C_d as the number of cycles of $\vec{B}_{xy}$ required to generate a droplet. The parameter C_d is constant for arrays that have constant droplet-to-droplet spacing. There is a minimum of one full cycle of $\vec{B}_{xy}$ required to generate a single droplet ($C_d = 1$). For decreasing ΔP, more cycles are required for the generation of a single droplet ($C_d \geq 1$), resulting in droplet arrays that are less tightly spaced (Fig. 2b and Video 2 in Supplemental Material [28]). The parameter C_d is non-constant for arrays that have non-constant spacings between consecutive droplets, while still preserving a periodic pattern; for example there can be periodic alternation between one and two cycles per droplet (i.e. C_d exhibits sequence '..1-2-1-2..'), resulting in an average of $\bar{C}_d = 3/2$ (Fig. 2b). In these cases, the volumes of the droplets can also be different.

Model − To explain the different droplet-to-droplet spacing and individual droplet volumes in our generated arrays (Fig. 2b), we develop a theoretical model. We write a tractable expression for the magnetostatic energy of the droplet, which theoretically is defined as $U = \int -\vec{M} \cdot \vec{B}_{bar} dV$, where $\vec{M}$ is the magnetization of the droplet, $\vec{B}_{bar}$ is the magnetic field generated by the bars (Fig. 1a) and V is the volume of the droplet. To simplify the complicated expression for U (Section III in Appendix), we base our model on the following five assumptions: First, we consider the droplet as a point mass and write $U = -\vec{M} \cdot \vec{B}_{bar} V$. Second, we assume that $\vec{M} = M\hat{z}$ with V increasing linearly over time t for a given flow rate Q, allowing us to write the magnitude of the magnetic moment $\vec{\mu} = \vec{M} V$ as $\mu(t) = MQt$. Third, we assume that $\vec{B}_{bar}$ varies as a sine wave over time, consistent with the oscillatory nature of $\vec{B}_{xy}$, and write $\vec{B}_{bar} = B_{bar}\hat{z}$ where $B_{bar}(t) = B_0 sin(\omega t + \varphi_i)$ with $B_0 > 0$ being the maximum amplitude of $\vec{B}_{bar}$, ω the angular frequency, and φ_i the phase of $\vec{B}_{xy}$. Fourth,
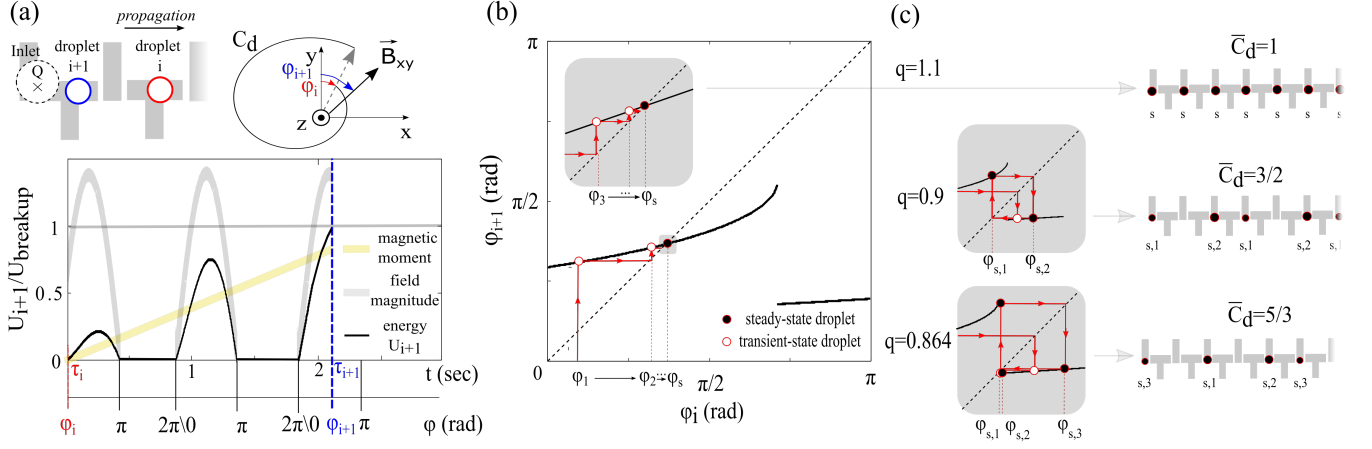
FIG. 3: (a) Schematic for recursive model. Assuming that the droplet 'i' (red) is generated at time $t = \tau_i$ when $\overrightarrow{B}_{xy}$ is at ϕ_i, the next droplet 'i+1' (blue) will be generated at $t = \tau_{i+1}$ and ϕ_{i+1}, when the energy of droplet 'i+1' becomes $U_{i+1} = U_{breakup}$, after a number of cycles $C_d = 1, 2, ..$ (black spiral), based on equation (2). U_{i+1} (black) is the total product of the normalized magnetic moment qt (yellow) and normalized magnetic field $f(t, \varphi_i) = \max(sin(2\pi t + \varphi_i), 0)$ (gray). (b) Plot of ϕ_{i+1} versus ϕ_i (solid black curve) based on the solution of equation (2) for q=1.1. The dashed line indicates the $y = x$ line and the red lines indicate the convergence of initial random ϕ_1 of transient-state droplets (white circles), to a ϕ_s of steady-state droplets (black circle). The gray inset shows a zoomed-in graphical solution converging to ϕ_s. (c) Graphical solutions of ϕ_{i+1} versus ϕ_i for $q = 1.1,\ 0.9,\ 0.864$ corresponding to $\bar{C}_d = 1, 3/2, 5/3$ with respective illustrations of sizes and spacings of droplets.

we assume that a droplet breaks up from the bulk when its energy U is minimized to a threshold $U_{breakup}$ which has no effective dependence on droplet volume based on geometric calculations (Section V in Appendix). Additionally, for the rest of this work, we will refer to the absolute value of the energy U. Fifth, we assume that droplet breakup can occur only in the attractive phase of the oscillation when $sin(wt + \varphi) > 0$ and $B_{bar}(t) > 0$. In the repulsive phase, the droplet is pushed away from the magnetized bar, which then reduces the applied magnetic force on the droplet, preventing breakup from occurring.

Combining all five of these assumptions, we write down the equation for the magnetostatic energy of the model as:

$$U(t) = \begin{cases} B_0 MQt sin(\omega t + \varphi) & ,\ sin(\omega t + \varphi) \geq 0 \\ 0 & ,\ sin(\omega t + \varphi) < 0 \end{cases} \quad (1)$$

Once a droplet is released, only the phase of $\overrightarrow{B}_{xy}$ at the previous breakup is needed to determine the time to next breakup. This allows us to write equation (1) as a recursive formula; assuming that a droplet 'i' is generated at time $t = \tau_i$ when $\overrightarrow{B}_{xy}$ is at angle φ_i, then the next droplet 'i+1' will be generated at time $t = \tau_{i+1}$ and ϕ_{i+1}, which occurs when the droplet magnetic energy is equal to $U(\tau_{i+1}) = U_{i+1} = U_{breakup}$ (Fig. 3b). Without loss of generality, we reduce equation (1) by setting $B_0 MQ = q$ (s^{-1}), $\omega = 2\pi\ (rad/sec)$ and $U_{breakup} = 1$, and write the recursive expression as:

$$q\tau_{i+1} F(\tau_{i+1},\ \varphi_i) = 1 \quad (2)$$

Where F is the waveform of the magnetic field relevant for breakup, and is given by $F(t,\ \varphi_i) = \max(sin(2\pi t + \varphi_i), 0)$ (Fig. 3a, gray field magnitude curve). Next, we solve equation (2) to reproduce the phenotype of the droplet arrays generated experimentally (Fig. 2b). For given q and angles φ_i in the range $[0, \pi]$, we find the corresponding values of τ_{i+1}. We restrict our parameter range for φ_i to an upper bound of π since no breakup can occur from π to 2π. Then, we calculate both the angle φ_{i+1} based on equation $\varphi_{i+1} = \mathrm{mod}_{2\pi}(2\pi\tau_{i+1} + \varphi_i)$ and the number of cycles C_d required to generate a droplet 'i+1' based on $C_d = \mathrm{quotient}_{2\pi}(2\pi\tau_{i+1} + \varphi_i)$, therefore generating phase maps for specific q values that relate φ_i to φ_{i+1} (Fig. 3b,c). For $q = 1.1$, φ_i converges to a single steady-state angle φ_s (Fig. 3b) resulting in monodisperse limit cycles of droplets with $\bar{C}_d = 1$ (Fig. 3c) independent of the initial φ_0. In other cases, for example at $q = 0.9$ and $q = 0.864$, φ_i periodically alternates respectively between two and three steady-state angles (Fig. 3c) resulting in multidisperse limit cycles of droplets with average $\bar{C}_d = 3/2$ ($C_d = .., 2, 1, ..$) and $\bar{C}_d = 5/3$ ($C_d = .., 2, 2, 1, ..$) in qualitative agreement with experiments (Fig. 2b).

To study the stability and pattern-space of the model, we conduct a parameter sweep of q in the range: $[0.15, 1.5]$ (Fig. 4). The phase-stability map reveals (steady-state) limit cycles of two types: the first concerns monodisperse limit cycles with integer $\bar{C}_d$ values (Fig. 4a; black lines for which $\varphi_i = \varphi_{i+1}$), and the second concerns multidisperse limit cycles with non-integer $\bar{C}_d$ values (Fig. 4a; red lines). These multidisperse limit cycles occur at discontinuous boundaries in the phase map (qualitatively as in Fig. 3c, $\bar{C}_d = 3/2,\ 5/3$). In addition,
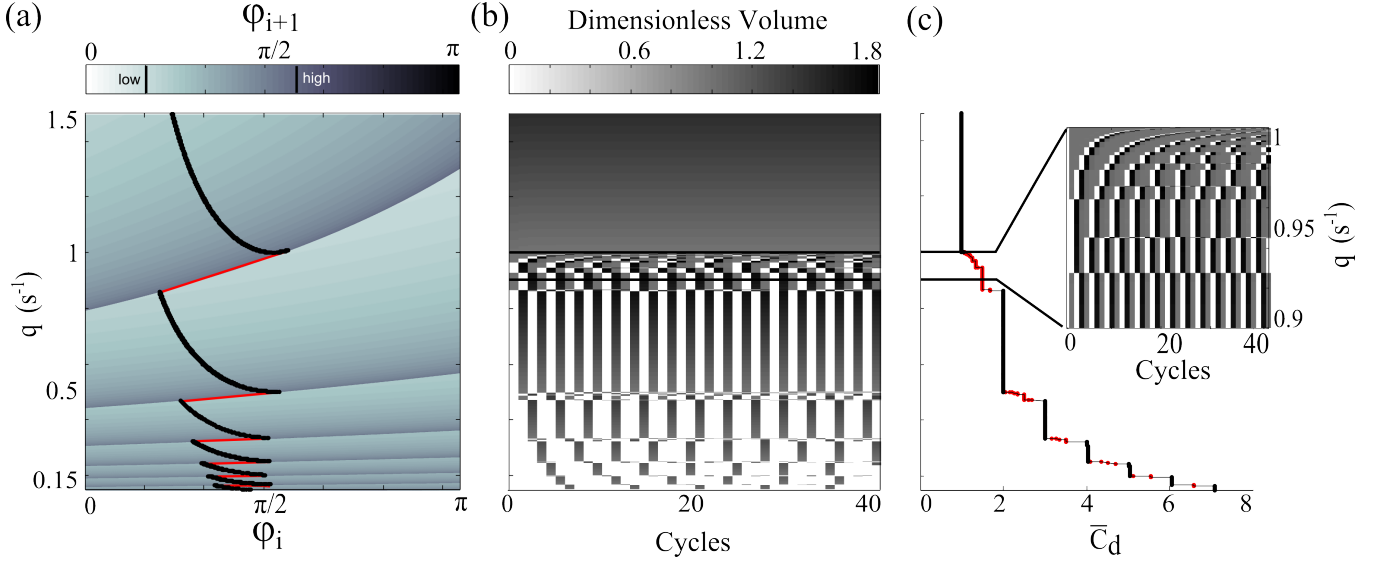
FIG. 4: Simulation parameter sweep of equation (2). (a) Phase map where each row corresponds to a mapping from φ_i (x-axis) to φ_{i+1} (colorbar), for a given flow rate q. The black lines correspond to monodisperse limit cycles of droplets where phase maps intersect the unity lines with positive slope at exactly one point. Red lines denote multidisperse limit cycles of droplets for $\varphi_i \rightarrow \varphi_{i+1}$ mapping. Low and high bounds in colorbar correspond to mapping limits given any initial φ_i. (b) Plot of droplet volumes for discrete cycles of $\vec{B}_{xy}$ as a function of flow rate (q). White cells indicate cycles where no droplet was generated. Cell shade indicates dimensionless droplet volume at a given cycle (colorbar). (c) Plot of $\bar{C}_d$ as a function of q. Red dots correspond to regions of multiple stead-state points as in (a).

for the explored parameter range, we find that given any initial φ_i value, the subsequent φ_{i+1} is always narrowed to a band of $[0.509, \ 1.771] \ rad$ (Fig. 4a, colorbar).

Furthermore, to illustrate the richness in potential droplet spacing and volume patterns, we calculate droplet volume over discrete cycle intervals at different q values (Fig. 4b). The pattern-space includes monodisperse and multidisperse droplet sequences at $\bar{C}_d$ (Fig. 4c) values observed experimentally (Fig. 2c).

Comparison of experiment and model − To understand the relationship between the droplet volume and pressure, we study one configuration at an in-plane frequency $f = 2 \ Hz$, describe the measured physical quantities in detail and test our analytic model by comparing to the experimental results (Fig. 5).

Decreasing pressure down from $8 \ kPa$, we find monotonically increasing $\bar{C}_d$ values (Fig. 5a). For a given $\bar{C}_d$ value, average droplet volume decreases with decreasing pressure. As $\bar{C}_d$ transitions from 1 to 2, 2 to 3/2 and 3/2 to 3, droplet volumes jump abruptly to higher values before decreasing again (Fig. 5b). We find that the average minimal droplet volume for all integer $\bar{C}_d$ is $V_{min} = 0.059\mu l$ (Fig. 5b, dashed line). Plotting the flow rate, $Q = V_{drop}f/\bar{C}_d$, as function of ΔP gives a linear relationship with a slope of $26.2 * 10^{-3} \ \mu l \ s^{-1} \ kPa^{-1}$ (Fig. 5c, $R^2 = 0.997$). The linearity of this relationship confirms that the flow rate Q of the FF is determined by the pressure difference ΔP as typically seen in Hagen-Poiseville flow [29] where there is a balance between viscous and pressure forces. Given this balance, the mag-

netic force from the bars, and the interfacial forces at the exit of the inlet tube determine the breakup of the supplied fluid volume to generate droplets with certain volumes and spacings.

Given the experimentally determined V_{min}, we can reevaluate equation (2) and compare theory to experiment, by parameterizing $q = Q/V_{min}$ and setting $\omega = 2 * 2\pi$. We use the recursive equation (2) to numerically solve exact values of $\bar{C}_d$ (Fig. 5a, gray line) and the droplet volumes (Fig. 5b) for $V_{min} = 0.059 \ \mu l$ over a range of q. With V_{min} as the single-parameter fit, we find good qualitative agreement between experiment and theory, particularly in the transitions between different $\bar{C}_d$. For $\bar{C}_d = 3/2$, we find a difference in expected droplet volumes suggesting that there may need to be important corrections made to the B_{xy} waveform.

Conclusions − In summary, we have demonstrated an experimental platform in which a periodic force generates droplet arrays with complex patterns of droplet spacings and sizes. We have developed a discrete-time dynamical systems model to explain the observed patterns, and found good agreement with experimental measurements. In future efforts, we can extend our system to quantitatively describe generation of droplet patterns by exploring the system's rich parameter space including the interfacial tension, the magnitudes of the magnetic fields, the frequency of the rotating magnetic field and by studying the transient behavior of the system as well. Our theoretical framework may be of broad interest due to its generic nature and the ability to be applied to other droplet gen-
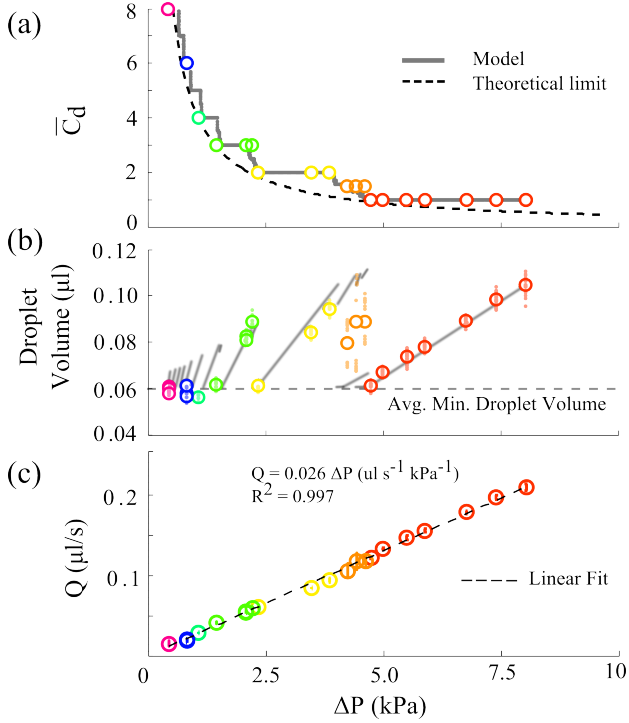
FIG. 5: Experimental droplet generation. (a)Plot of $\bar{C}_d$, over pressure ΔP. Colors serve as a legend for panels (b) and (c). Dashed black line is the theoretical minimum of $\bar{C}_d$ given the average minimum droplet volume ($V_{min} = 0.59\mu l$). Gray line is fit of $\bar{C}_d$ from the solution of equation (2) given a single-parameter fit using V_{min}. (b) Droplet volumes as a function of pressure. Large colored circles are average values for generated droplet volumes at a given pressure. Smaller colored dots correspond to individual droplet volumes. Dashed horizontal line is the average minimum droplet volume. Gray lines are values of droplet volumes from model solutions given V_{min}. (c) Plot of Flow rate over ΔP with linear fit.

to reference [27]. The 'T' and 'I' bars have millimeter-size dimensions (Table I). The permalloy bars are coated with teflon and the fluidic chips do not have a top cover.

TABLE I: Table with nominal dimensions of 'T' and 'I' bars

Dimensions of 'T' and 'I' bars	(μm)
l_1	1012.5
l_2	1125
l_3	1125
w	213.5
t	25
g	70

Magnetic fields − The magnetic fields are generated using the system of electromagnetic coils described in reference [27]. The ratio between the magnitudes of the magnetic fields is $\mid B_z \mid / \mid B_{xy} \mid \geq 5$, thus ensuring that the induced magnetization of the generated droplets is along the z-axis (Fig. reffig:schematica). However, the induced magnetization of the metallic bars is always in the x-y plane as they are too thin (for example $t/l_1 = 1/40$) to support magnetization in the z-axis (Fig. 1a).

Two-phase mixture of fluids − The mixture consists of two phases. The first phase is silicone oil (Sigma Aldrich, CAS: 63148-62-9, kinematic viscosity 5 cSt, density 0.913 kg/m^3) which is pipetted on the surface of the fluidic chip forming a film of thickness $h_{oil} = 3 - 5mm$ beneath the open air-oil interface. The second phase is water-based ferrofluid (Ferrotec EMG 700, kinematic viscosity 5 cSt, density 1.28 kg/m^3) which is dispensed on the film using an inlet tubing (Fig. 1a).

Inlet tubing − The inlet tubing is made of teflon (PTFE) with internal diameter 300 μm and length 1 m. The first tip of the tubing is suspended at a height $d = 50 - 200 \mu m$ above the permalloy bars. This height d is always smaller than the thickness of the silicone oil film on the substrate, that is $d < h_{oil}$, thus making this tip completely immersed in the film. The second tip of the tubing is connected to a ferrofluid reservoir whose top surface is at a height $h_{ff} = 10 - 80\ cm$ above the permalloy bars. This height h_{ff} creates a pressure difference ΔP generating flow that fills the tubing with ferrofluid and - via the first tip - dispenses it into the substrate. The pressure difference ΔP is adjusted by adjusting the height h_{ff} of the ferrofluid reservoir. Furthermore, the inlet tubing is threaded through a glass capillary with internal diameter 500 μm, which is mounted on a three-axis translational stage for adjusting the position of the end of the inlet tubing relative to the permalloy bars. The height of the oil (h_{oil}) contributes an insignificant

eration platforms driven acoustically, (di)electrically, or magnetically, and in a more complex fashion with arbitrary forcing functions or multiple drive time scales. We note that the phase space accessible in this class of problems is rich and will inspire new experimental platforms replicating these results in other systems.

Appendix

I. EXPERIMENTAL METHODS

Fabrication of fluidic chips − The 'T' and 'I' bars are fabricated by etching permalloy foils that are epoxy-bonded on glass substrates, using an protocol identical

reduction in pressure and is not considered here. It is also important to note that the open geometry microfluidics ensures that once a droplet has broken from continuous phase, droplets do not generate a significant backpressure as seen in narrow channel based microfluidic systems.

In our system, the relevant capillary forces are $F_{cap} \approx \gamma \, d_{tube} \approx 3\mu N$, where γ is the interfacial tension between the ferrofluid and the silicone oil, and the shearing forces from the magnetic fields are $F_{mag} \approx 10\mu N$ for droplets with radius of roughly $250\mu m$ [27], suggesting comparable force scales for droplet breakup. However, both the capillary and magnetic forces are small in comparison to the force exerted on the droplet by line pressure ($F_{line} \approx 50 - 500\mu N$). This estimation suggests a constant flow and constant pressure regime.

Outlet tubing − The outlet tubing is made of teflon, similar to the inlet tubing (Fig. 1a). At its lower end that is in proximity to the substrate, it also contains a blunt-tip pin made of stainless steel (23 gauge). The magnetic field $\overrightarrow{B}_z$ along the z-axis magnetizes the pin. The magnetized pin attracts the ferrofluid droplets and by also using an additional negative pressure difference across the outlet tubing, the droplets that reach the outlet tubing are removed from the substrate (Fig. 1, Fig. A1, and Fig. A2).

Imaging − Droplet volume measurements are performed by imaging the chip with a dSLR (Canon T3i, Canon EF 100mm f/2.8L IS USM Macro Lens).

PTFE-Oil-Ferrofluid Surface Energy. In order to estimate the volume of sessile droplets, by only imaging from the top, we measured the contact angle between ferrofluid, PTFE in silicone oil. We measured 11 droplets from the side, sessile on a PTFE surface, for an average surface angle of $\theta = 24.86 \pm 2.72$ (Fig. A3).

II. DATA ANALYSIS

Droplet Volume Measurement. For each measurement, droplets are first generated and then all B-fields are turned off, so that the droplets are in a sessile state on the chip surface. The droplets are automatically tracked using a custom image analysis code written in MATLAB [27]. The code converts the frames of the videos to grayscale values from 0 to 1. Due to the opacity of the ferrofluid, a brightness threshold is easily selected to identify one contiguous droplet object. To extract the radii of the droplets, circles are interpolated on the droplets. For maximal droplet volumes of $V_{droplet} \approx 0.12 \, ul$, the Bond number is $Bo \approx 0.25$ ($\Delta\rho = \rho_{ff} - \rho_{oil} = 0.2g/ml$; $\gamma = 3 \, mN/m$ [30], therefore justifying the spherical cap assumption in calculating the volumes of the droplets, where $V_{cap}(r,\theta) = (\pi r^3/6)(1-cos\theta)(3sin\theta^2+(1-cos\theta)^2)$.
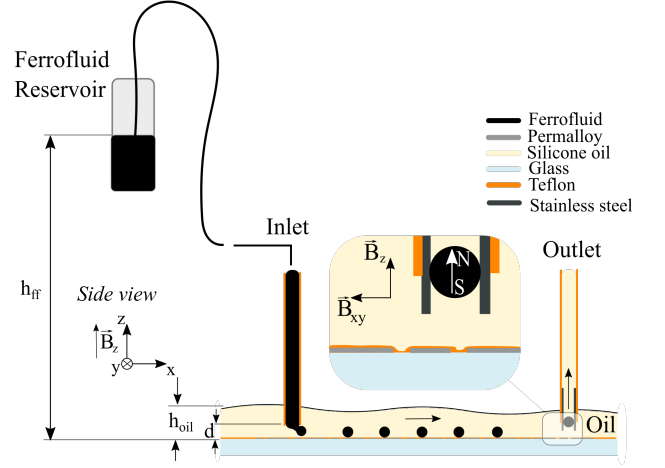

FIG. A1: Schematic of droplet generator. *Side view*: The inlet tube contains a FF column (black) with controllable hydrostatic pressure set by the height, h_{ff}. The droplets propagate on the tracks covered with silicone oil with height h_{oil} and exit the substrate through an outlet tube (shown in inset) connected to a negative pressure line.
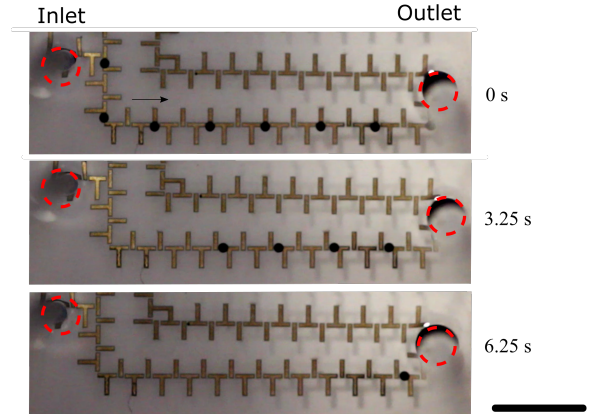

FIG. A2: Top-view sequential snapshots of a experiment where generated droplets propagate on winding tracks of 'T' and 'I' bars and are removed from the substrate through the outlet. Red dashed circles indicate the inlet and outlet. $B_n = 250 \, G$, $B_i = 40 \, G$ at frequency $f = 2 \, Hz$. Scale bar $5mm$.

III. MODEL AND FITS

Computational Solution. MATLAB R2014a was used to numerically solve the recursive equation (2). The recursive process is as follows: after the i-th droplet is generated, time is reset to $t = 0$ and φ_i is propagated to the subsequent iteration. We next solve for the time, τ_{i+1}, that it takes for the energy to reach $U_{breakup}$. To plot phase maps, we solve the recursive equation for a range of φ from 0 to π in increments of at least 0.001.

Model Simplification. The full expression of U is challenging to calculate because $\overrightarrow{B}_{bar}$ depends on the relative
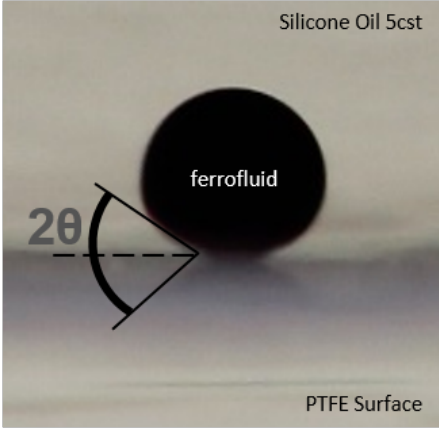
FIG. A3: A sessile ferrofluid droplet resting on a glass-PTFE spun coat surface in 5cst silicone oil. Image taken from the side. The droplet radius is approximately $300\mu m$.

position of the inlet tubing with respect to the tracks, as well as the track's materials and geometry. $\overrightarrow{B}_{bar}$ also changes spatiotemporally with gradients of similar length scale as the dimension of the tracks. In addition, $\overrightarrow{M}$ is affected by $\overrightarrow{B}_{bar}$ while the volume and shape of the droplet also change over time.

Simple Theoretical Derivation of Upper Phase Band Limit. Though the model is nonlinear and we were not able to find a close-formed solution for the stable points, we have derived an expression for the upper bound of φ_{i+1} given any initial φ_i. The upper limit comes from the fact that any droplet that does not breakup before the maximum in the energy waveform, has to wait until the next cycle to breakup. The theoretical upper limit for the band is given by the solution to the equation: $0 = d/dx(t\sin(wt)) = \sin(wt) + wt\cos(wt)$, which gives $\varphi_{upper} = 2.0287... \, rad$ for $w = 2\pi$.

Simple Theoretical Derivation of $\bar{C}_d$ Lower Bound. To find the bound of $\bar{C}_d$, we take $\sin(w\tau_{i+1} + \varphi_i) \to 1$, which gives a simple relationship of $\tau = V_{min}/Q$, giving a lower limit of $\bar{C}_d > V_{min}f/Q$ (Fig. 5a, black dashed line). The agreement with the bound across the pressure range confirms that V_{min} is not significantly varying as a function of Q.

Fitting. Linear fitting was done using the first-order Polyfit function in Matlab. R^2 value was then calculated as an estimator of linearity.

IV. INFLUENCE OF DROPLET SIZE ON BREAKUP ENERGY

When a droplet of volume V and surface area S breaks from the column of fluid at the lower end of the inlet tube (Fig. 1a), there is an increase ΔS of the area of the ferrofluid-oil interface:

$$\Delta S = S_{post-breakup} - S_{pre-breakup} \tag{A1}$$

In equation (A1) the terms $S_{pre-breakup}$ and $S_{post-breakup}$ are the equilibrium areas of the ferrofluid-oil interface before and after break-up respectively. Only taking into account the two equilibrium states, the energy of breakup $U_{breakup}$ is proportional to the difference between these areas for a given interfacial tension γ:

$$U_{breakup} = \gamma \Delta S \tag{A2}$$

We estimate these areas $S_{pre-breakup}$ and $S_{post-breakup}$ using two geometric assumptions:

First, we assume that, before droplet breakup, the fluid volume at the tip has the shape of a spherical cap defined by the height of the cap h and the cap radius which is equal to inner radius the inlet tube a. This assumption is justified as the Bond number for this system is $Bo \approx 0.25$ (see section II). Therefore, the cap has a surface area $S = \pi(a^2 + h^2)$ and a volume $V = \pi h(3a^2 + h^2)/6$. Next, we combine these two equations by substituting h and through algebraic calculations we write:

$$S^3 + [3a^2\pi]S^2 + [-36V^2\pi - 4a^6\pi^3] = 0 \tag{A3}$$

The root of equation (A3) gives the surface area of the spherical cap for given volume V and inlet radius a, that is $S_{pre-breakup} = S(V, a)$.

Second, we assume that, after droplet breakup, the fluid volume that used to be a cap, is now a free droplet with volume $V = \pi d^3/6$ and surface area $S = \pi d^2$ where d is the droplet diameter. In addition, the newly formed interface at the tip after the breakup has a flat circular surface equal to the cross-section of the inlet tube with radius a with area πa^2. Therefore, we write the area of the ferrofluid-oil interface after the droplet breakup as a function of V and a as:

$$S_{post-breakup} = \pi^{1/3}(6V)^{2/3} + \pi a^2 \tag{A4}$$

Next, we evaluate equation (A2) by taking $S_{pre-breakup}$ as the root for equation (A3) and evaluating $S_{post-breakup}$ from equation (A4) for a fixed radius of inlet tube $a = 150$ μm (see section I) and a range of droplet volumes $V = 0.00 - 0.15\mu l$ (Fig.A4). We observe that in our experimental range of droplet volumes $V = 0.06 - 0.12\mu l$ the difference in surface area varies within less than 3% (Fig.A4)

Due to the small variation in the surface area before and after-break up within our experimental range, the variation of breakup energy is also small. For a given $\gamma = 3mN/m$, $V_1 = 0.06\mu l$, and $V_2 = 0.12\mu l$, we calculated respectively from equations (A2, A3, A4), $U_{breakup,1} = 40.3$ nJ and $U_{breakup,2} = 41.3$ nJ, which have a relative difference of 2.4%, thus justifying our assumption that the threshold for energy breakup can be assumed to be constant.
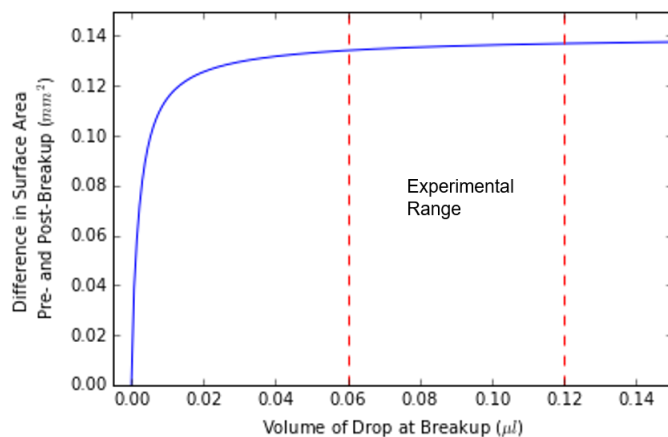
FIG. A4: Surface area difference between the oil-ferrofluid interface pre- and post-breakup. Red dashed lines are the bounds on droplet volumes observed experimentally.

[1] M. G. Neubert, M. Kot,and M. A. Lewis, Theoretical Population Biology **48**, 7 (1995).

[2] X. Liu, and D. Xiao, Chaos, Solitions & Fractals **32**, 80 (2007).

[3] M. Kot, Journal of mathematical biology **302**, 413 (1992).

[4] K. Ogata, *Discrete-time control systems,*Vol. 2 (Prentice Hall Englewood Cliffs, NJ, 1995).

[5] I. Campos-Canton, E. Campos-Canton, J. Murguía, and H. Rosu, Chaos, Solitons & Fractals **42**, 12 (2009).

[6] T. Yoshida, H. Mori, and H. Shigematsu, Journal of statistical physics **31**, 279 (1983).

[7] S. H. Strogatz, *Nonlinear dynamics and chaos: with applications to physics, biology, chemistry, and engineering,* (Westview press, 2014).

[8] R. M. May, Nature **261**, 459 (1976).

[9] P. Martien, S.C. Pope, P.L. Scott,and R.S. Shaw, Physics Letters A **110**, 399 (1985).

[10] P. Garstecki, M. J. Fuerstman, and G. M. Whitesides, Nature Physics **1**, 168 (2005).

[11] D. Sessoms, A. Amon, L. Courbin, and P. Panizza, Physical review letters **105**, 154 (2010).

[12] R. Link, J.P. Vest, and D. Bartolo, Physical review letters **108**, 034501 (2012).

[13] J. A. Schwartz, J.V. Vykoukal, and P.R. Gascoyne, Lab on a Chip **4**, 11 (2004).

[14] H. Song, J. Chen, and R.F. Ismagilov, Angewandte-chemie international edition **45**, 7336 (2006).

[15] S.-Y. Teh, R. Hung, and A. P. Lee, Lab on a Chip **8**, 198 (2008).

[16] T. Schneider, J. Kreutz, and D. T. Chiu, Analytical chemistry **85**, 3476 (2013).

[17] T. Thorsen, R. W. Roberts, F. H. Arnold, and S. R. Quake, Physical review letters **86**, 4163 (2001).

[18] P. Garstecki, M. J. Fuerstman, H. A. Stone, and G. M. Whitesides, Lab on a Chip **6**, 437 (2006).

[19] D. Link, S. L. Anna, D. Weitz, and H. Stone, Physical review letters **92**, 054503 (2004).

[20] K. Kita, M. Ichikawa, and Y. Kimura, Physical Review Letters E **77**, 041702 (2008).

[21] J.V. Timonen, M. Latikka, L. Leibler, R. H. Ras, and O. Ikkala, Science **341**, 253 (2013).

[22] G.F. Christopher, and S.L. Anna, Journal of Physics D: Applied Physics **40**, 319 (2007).

[23] J.D. Tice, H. Song, A.D. Lyon, and R.F. Ismagilov, Langmuir **19**, 9127 (2003).

[24] S. L. Anna, N. Bontoux,and H.A. Stone, Applied physics letters **82**, 364 (2003).

[25] P. Garstecki, H. A. Stone, and G. M. Whitesides, Physical review letters **94**, 164501 (2005).

[26] W. Li, E. W. Young M. Seo, Z. Nie, P. Garstecki, C.A. Simmons, and E. Kumacheva, Soft matter **4**, 258 (2008).

[27] G. Katsikis, J. S. Cybulski,and M. Prakash, Nature Physics **11**, 588 (2015).

[28] See Supplemental Materials at [URL will be inserted by publisher] for videos showing the operation of the droplet generator.

[29] F.M. White, Viscous fluid flow, Mac Graw, New York, (1991).

[30] C. Flament, S. Lacis, J-C. Bacri, A. Cebers, S. Neveu,and R.. Perzynski, Physical Review E **53**, 4801 (1996).